Accurate Loop Gain Modeling of Digitally Controlled Buck Converters

Lin, Jianheng; Su, Mei; Sun, Yao; Li, Xing; Xie, Shiming ; Zhang, Guanguan; Blaabjerg, Frede; Feng, Jianghua

Published in:
I E E E Transactions on Industrial Electronics

DOI (link to publication from Publisher):
10.1109/TIE.2021.3050389

Publication date:
2022

Document Version
Accepted author manuscript, peer reviewed version

Accurate Loop Gain Modeling of Digitally Controlled Buck Converters

Jianheng Lin, Mei Su, *Member, IEEE,* Yao Sun, *Member, IEEE*, Xing Li, Shiming Xie, Guanguan Zhang, Frede Blaabjerg, *Fellow, IEEE*, and Jianghua Feng

***Abstract*—For the digitally controlled Buck converters, the nonlinearity and time-periodicity, caused by the pulse-width modulator (PWM) and sample-and-hold, make the accurate frequency-domain analysis intractable. In this paper, based on the harmonic transfer function (HTF) approach, a precise small-signal continuous-time modeling for the digitally controlled Buck converter operating in continuous-conduction mode (CCM) under constant-frequency voltage-mode control is presented. The sideband components on the closed-loop control are embedded in the model. Thus, this model is accurate within the full frequency domain region, which breaks the limit of Nyquist frequency. Furthermore, by overcoming the barrier of infinite series introduced by the sideband effects, the analytical loop gain expression is derived, which contributes to accurate stability assessment and reduction of computation burden. In addition, the proposed exact small-signal model has explained the reasons why different information injection points lead to different measured loop gains. Simulations and experimental results are conducted to verify the effectiveness of the proposed method.**

***Index Terms*—Digital control, loop gain measurement, sideband effects, time-periodicity.**

I. Introduction

THE REDUCED PRICES and improved performance of digital controllers have been paid increasing attention for switching power converters [1]. The digital control possesses some advantages including noise immunity, programmability, as well as the possibility to implement sophisticated control [2]. Owing to the application of Pulse-Width Modulator (PWM) and sample-and-hold, the digitally controlled switching power converter systems are characterized by nonlinearity and time-periodicity [3].

In order to deal with nonlinearity and time-periodicity, many modeling techniques of power converters have been developed. The discrete-time modeling technique, which was introduced in [4], is a popular choice. The discrete-time model is accurate for stability prediction, which is mainly used to analyze nonlinear phenomena such as chaos and bifurcation [5]. However, the discrete-time model has abandoned the usual continuous-time representation, no information concerning the intra-cycle waveform propagation is retained. As a result, the discrete-time models approximate the time domain response of the system [6].

In another direction, continuous-time modeling methods have also been greatly developed, which have been successfully applied in circuit and controller design [7]. The averaging technique is the most widely used method for deriving the continuous-time transfer function of PWM converters, proposed by Middlebrook and Cuk in [8], which only considered the DC component over a switching cycle. The averaging technique is easy to be implemented, and it permits the Linear-Time-Invariant (LTI) theory to be used for the nonlinear system analysis [9]. However, due to the neglect of switching details, the average model fails to provide accurate stability prediction of the closed-loop PWM converters, laying a potential risk for system operation [10].

In order to improve the accuracy of the continuous-time model, the coupling dynamics of sideband components should be incorporated into the closed-loop modeling. The Generalized State-Space Averaging (GSSA) modeling method is an efficient approach to capture the high-order harmonics of the switching power converters [11]. After being validated, GSSA has been successfully extended to study the sideband effects of PWM converters [12]-[14]. Most of these studies rely on computer programs because of a lot of calculations. In order to obtain a result with physical insight, simplified versions of this method have been developed. Besides the component at the fundamental perturbed frequency, the two-frequency model in [15]-[16] considered the sideband component at another perturbed frequency. An extension, denoted as the four-frequency model, took four sideband components into

Manuscript received September 18, 2020; revised December 5, 2020; accepted December 25, 2020. This work was supported in part by the Hunan Provincial Key Laboratory of Power Electronics Equipment and Grid under Grant 2018TP1001, in part by the National Natural Science Foundation of China under Grant 61933011, 61903222, 51807206, in part by the Project of Innovation-driven Plan in Central South University under Grant 2019CX003, in part by the CRRC Zhuzhou Electric Locomotive Institute Co., Ltd. (YJYJS2018-017). (Corresponding author: Yao Sun).

J. Lin, M. Su, Y. Sun, and S. Xie are with the School of Automation, Central South University, Changsha 410083, China (e-mail: mltortoise@163.com; sumeicsu@csu.edu.cn; yaosuncsu@gmail.com; shimingxie@csu.edu.cn).

X. Li is with the College of Electrical and Information Engineering Hunan University, Changsha 410082, China (e-mail: lxhnu@hnu.edu.cn).

G. Zhang is with the School of Control Science and Engineering, Shandong University, Jinan 250013, China (e-mail: dr_zgg@163.com).

F. Blaabjerg is with the Department of Energy Technology, Aalborg University, 9220 Aalborg, Denmark (e-mail: fbl@et.aau.dk).

J. Feng is with the CRRC Zhuzhou Institute Co. Ltd., Zhuzhou 412001, China (e-mail: fengjh@csrzic.com).

consideration, which improved the model accuracy in the high-frequency regions [17]. In [18], a matrix-based multi-frequency model is proposed, which is able to capture all the sideband components. Multi-Input Multi-Output (MIMO) analysis tools are required for the matrix-based model. In order to achieve high accuracy while preserving Single-Input Single-Output (SISO) form, an extended-frequency modeling method is proposed by Li in [19]. However, the accurate analytical form of the extended-frequency model is not given. By selecting optimally the dominant sideband component, a satisfied balance between complexity and accuracy can be achieved by the generalized multi-frequency small-signal model in [20].

Existing studies are mostly focused on modeling PWM converters under analog control, where only the PWM produces the sideband effects [12]-[20]. However, the inherent sample-and-hold in digital control also results in sideband effects, which strongly complicates converter modeling. Although the discrete-time modeling technique is mature in modeling digitally controlled converters, an accurate continuous-time model of the digitally controlled converter is still missing here, therefore this paper aims to bridge this gap. The conventional controller design method based on the cutoff frequency and phase margin can be applied directly to the continuous-time model.

Moreover, in the experiment, it was observed that for a simple digitally controlled converter, different injection points led to different loop gain measurement results [21]-[22]. However, due to the lack of an accurate continuous-time model of the digitally controlled converter, the difference in loop gain measurement results caused by different injection points has not been clearly understood [23]. The details are discussed in Section III-D. This is also one reason motivating the authors to do the work of this paper.

Considering the time-periodicity caused by the PWM and sample-and-hold, a more general modeling method is required. In this aspect, the Harmonic-State-Space (HSS) modeling method [24] and the Harmonic-Transfer-Function (HTF) modeling method [25], rested on Linear-Time-Periodic (LTP) theory, are promising choices. The HSS modeling method has been widely adopted to study the interactions between different sideband components [26]-[27]. The HSS model maps the LTP model into an infinite-dimensional LTI model with a state-space-like form. And the model accuracy is improved by expanding the dimensions of the HSS model. Because of the large dimensions of the HSS model, it is difficult to transform the HSS model into a transfer-function-like model directly [28]. In this regard, the HTF approach is the appropriate one to derive the frequency-domain model of the LTP system, which uses a transfer function matrix to describe the relationship between inputs and outputs in different frequency domains [29]-[30]. Compared with existing modeling methods, the HTF approach is more general and retains clear physical insights. Based on the discussion aforementioned, the HTF approach is adopted in this paper for modeling the digitally controlled Buck system with consideration of the sideband effects.

The main contributions of the paper are summarized as:

1) The small-signal continuous-time modeling of digitally controlled Buck converters operating in Continuous Conduction Mode (CCM) under constant-frequency voltage-mode control, which considers the sideband effects, is presented. The obtained loop gain model is accurate within the full frequency domain region, which breaks the limit of Nyquist frequency.

2) The analytical loop gain expression is derived by overcoming the barrier of infinite series resulted from the sideband effects, laying the foundation for accurate stability assessment and a significant reduction in computation burden.

3) The reason that different information injection points lead to different measured loop gains is revealed. And the conditions for the right loop gain measurement are given.

The rest of the paper is organized as follows. In Section II, a brief review of the basic concepts of the harmonic transfer function approach is reported. In Section III, the continuous-time small-signal models of the PWM and sampling holder are derived, considering all the sideband components. Moreover, the loop gain of the digitally controlled Buck system is deduced, and the loop gain measurement schemes with different information injection points are analyzed. In Section IV, an analytical loop gain expression is derived and the conditions that the measured results are equal to the actual loop gain are given. In Section V, experiments are carried out, which shows in all cases good agreement with the analytical and simulation results. In Section VI, the conclusions of this paper are drawn.

II. Basic Concept of Harmonic Transfer Function

The harmonic transfer function approach established on the basis of LTP theory is one efficient tool to analyze the small-signal behavior of time-periodic systems. In order to capture all the possible frequency couplings, Exponential Modulated Periodic (EMP) signal is introduced in the HTF framework, which is defined as [24]

$$\tilde{u}(t)=\sum_{k=-\infty}^{\infty}\tilde{U}_k e^{jk\omega_0 t}e^{st} \tag{1}$$

ω_0 is the fundamental frequency of the system and $s=j\omega$ where ω denotes the frequency variable. The most important feature of EMP is that an LTP system maps EMP signals onto EMP signals, which contributes to the derivation of the transfer-function-like model as an LTI system.

A general LTP system can be represented by its impulse response $h(t, \tau)$ with its periodicity as

$$h(t,\tau)=h(t+T_0,\tau+T_0) \tag{2}$$

where $T_0=2\pi/\omega_0$. When an EMP signal is given as input to the LTP system, this gives the following output

$$\tilde{y}(t)=\sum_{k=-\infty}^{\infty}\tilde{U}_k e^{jk\omega_0 t}e^{st}\int_{-\infty}^{\infty}h(t,\tau)e^{-jk\omega_0\tau}e^{-s\tau}d\tau \tag{3}$$

The time-periodic transfer function is defined as

$$H(t,s)=\int_{-\infty}^{\infty}h(t,\tau)e^{-s\tau}d\tau \tag{4}$$

Then, the output can be rewritten as

$$\tilde{y}(t)=\sum_{k=-\infty}^{\infty}\tilde{U}_k e^{jk\omega_0 t}e^{st}H(t,s+jk\omega_0) \tag{5}$$

This article has been accepted for publication in a future issue of this journal, but has not been fully edited. Content may change prior to final publication. Citation information: DOI 10.1109/TIE.2021.3050389, IEEE Transactions on Industrial Electronics

According to Fourier transform, it gives that

$$\begin{cases} H(t,s+jk\omega_0) = \sum_{m=-\infty}^{\infty} H_m(s+jk\omega_0)e^{jm\omega_0 t} \\ H_m(s+jk\omega_0) = \frac{1}{T_0}\int_0^{T_0} H(t,s+jk\omega_0)e^{-jm\omega_0 t}dt \end{cases} \tag{6}$$

Substituting (6) into (5), it can lead to

$$\tilde{y}(t) = \sum_{n=-\infty}^{\infty}\sum_{k=-\infty}^{\infty} \tilde{U}_k H_{n-k}(s+jk\omega_0)e^{jn\omega_0 t}e^{st} \tag{7}$$

It is worth noting that the output signal is also an EMP signal

$$\tilde{y}(t) = \sum_{n=-\infty}^{\infty} \tilde{Y}_n e^{jn\omega_0 t}e^{st} \tag{8}$$

Rewriting (7) by matrix form yields

$$\begin{bmatrix} \vdots \\ \tilde{Y}_{-1} \\ \tilde{Y}_0 \\ \tilde{Y}_1 \\ \vdots \end{bmatrix} = \underbrace{\begin{bmatrix} \ddots & \ddots & \ddots & \ddots & \ddots \\ \ddots & H_0(s-j\omega_0) & H_{-1}(s) & H_{-2}(s+j\omega_0) & \ddots \\ \ddots & H_1(s-j\omega_0) & H_0(s) & H_{-1}(s+j\omega_0) & \ddots \\ \ddots & H_2(s-j\omega_0) & H_1(s) & H_0(s+j\omega_0) & \ddots \\ \ddots & \ddots & \ddots & \ddots & \ddots \end{bmatrix}}_{\mathcal{H}(s)} \begin{bmatrix} \vdots \\ \tilde{U}_{-1} \\ \tilde{U}_0 \\ \tilde{U}_1 \\ \vdots \end{bmatrix} \tag{9}$$

where $\mathcal{H}(s)$ is called the HTF of the LTP system. And HTF describes the input-output relation for an LTP system in different frequency domains.

Property 1: Given a general T_0-periodic multiplication operator

$$\tilde{y}(t) = A(t)\tilde{u}(t) \tag{10}$$

where $A(t)=A(t+T_0)$. Then the corresponding HTF is given as

$$\mathcal{A} = \mathcal{T}[A(t)] = \begin{bmatrix} \ddots & \ddots & \ddots & \ddots & \ddots \\ \ddots & A_0 & A_{-1} & A_{-2} & \ddots \\ \ddots & A_1 & A_0 & A_{-1} & \ddots \\ \ddots & A_2 & A_1 & A_0 & \ddots \\ \ddots & \ddots & \ddots & \ddots & \ddots \end{bmatrix} \tag{11}$$

where $\mathcal{T}[\cdot]$ represents the Toeplitz transform and A_k is the k_{th} Fourier coefficient of $A(t)$. $\mathcal{A}$ is called the Toeplitz matrix with respect to $A(t)$, which is a doubly infinite matrix.

Property 2: For an LTI system

$$\tilde{y}(t) = \int_{-\infty}^{\infty} g(\tau)\tilde{u}(t-\tau)d\tau \tag{12}$$

where

$$g(t) = \frac{1}{2\pi j}\int_{\sigma-j\infty}^{\sigma+j\infty} G(s)e^{st}ds \tag{13}$$

The resulting HTF format can be expressed as

$$\mathcal{G}(s) = \begin{bmatrix} \ddots & \ddots & \ddots & \ddots & \ddots \\ \ddots & G(s-j\omega_0) & 0 & 0 & \ddots \\ \ddots & 0 & G(s) & 0 & \ddots \\ \ddots & 0 & 0 & G(s+j\omega_0) & \ddots \\ \ddots & \ddots & \ddots & \ddots & \ddots \end{bmatrix} \tag{14}$$

As seen, the HTF of an LTI system only contains diagonal elements, which agrees with the fact that no frequency coupling exists in the LTI system.

Unlike the conventional LTI transfer function, the HTF is an infinite order transfer function matrix that captures the coupling among different frequencies that arise due to the periodic dynamics. Since the HTF maps an LTP system into an infinite-dimensional LTI space, the conventional analysis tools based on LTI theory can also be applicable to assess time-periodic systems.

III. Small-Signal Model of Digitally Controlled PWM Buck Converters

A. Pulse-Width Modulator Modeling

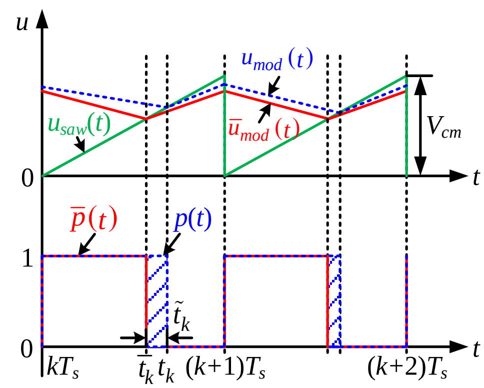

Fig. 1. Illustration of the pulse-width modulator.

Fig. 1 illustrates the input and output waveforms of the pulse-width modulator. At the k_{th} intersecting point of u_{mod} and u_{saw}, it satisfies the following equation

$$u_{mod}(t_k) = u_{saw}(t_k) \tag{15}$$

where t_k denotes the time instant of the intersection. And $u_{mod}(t)$ and $u_{saw}(t)$ are the modulation signal and carrier signal, respectively.

Suppose that the modulation signal $u_{mod}(t)$ consists of a steady-state part and a small-signal term

$$u_{mod}(t) = \bar{u}_{mod}(t) + \tilde{u}_{mod}(t) \tag{16}$$

where the superscript '~' and '-' represent the small-signal and steady-state quantities, respectively. Similarly, at the k_{th} cycle, if the steady-state intersecting time instant is $\bar{t}_k$, and the time instant perturbation is $\tilde{t}_k$, we have

$$t_k = \bar{t}_k + \tilde{t}_k \tag{17}$$

where

$$\bar{t}_k = kT_s + D_s T_s \tag{18}$$

and D_s is the steady-state duty cycle.

Substituting (17) and (18) into (16), it is derived that

$$\bar{u}_{mod}(\bar{t}_k + \tilde{t}_k) + \tilde{u}_{mod}(\bar{t}_k + \tilde{t}_k) = \frac{V_{cm}}{T_s}(\bar{t}_k + \tilde{t}_k) \tag{19}$$

where V_{cm} and T_s denote the amplitude and period of the carrier, respectively.

By taking the Taylor-series expansion of (19) and truncating at first order in small terms, it is straightforward to show that

$$\frac{V_{cm}}{T_s}(\bar{t}_k + \tilde{t}_k) = \bar{u}_{mod}(\bar{t}_k) + \frac{d\bar{u}_{mod}(\bar{t}_k)}{dt}\tilde{t}_k + \tilde{u}_{mod}(\bar{t}_k) \tag{20}$$

Eliminating the quiescent terms of (20) yields

$$\frac{d\bar{u}_{mod}}{dt}(\bar{t}_k)\tilde{t}_k + \tilde{u}_{mod}(\bar{t}_k) = \frac{V_{cm}}{T_s}\tilde{t}_k \tag{21}$$

Then the intersection time perturbation at k_{th} cycle can be

This article has been accepted for publication in a future issue of this journal, but has not been fully edited. Content may change prior to final publication. Citation information: DOI 10.1109/TIE.2021.3050389, IEEE Transactions on Industrial Electronics

derived as

$$\tilde{t}_k = \frac{T_s}{V_{cm} - T_s \dfrac{d\bar{u}_{mod}}{dt}\left(\bar{t}_k\right)} \tilde{u}_{mod}\left(\bar{t}_k\right) \tag{22}$$

The PWM pulse trains can be expressed as

$$p(t) = \sum_{k=0}^{\infty}\left[\varepsilon\left(t-kT_s\right) - \varepsilon\left(t-t_k\right)\right] \tag{23}$$

where $\varepsilon(x)$ is the step function [31]. Similarly, linearizing (23) and eliminating the quiescent terms of both sides give

$$\tilde{p}(t) = \sum_{k=0}^{\infty}\delta\left(t-\bar{t}_k\right)\tilde{t}_k \tag{24}$$

where $\delta(x)$ is the unit impulse function [31]. By substituting (22) into (24), an LTP mapping relationship is obtained as

$$\tilde{p}(t) = \frac{T_s}{V_{cm} - T_s \dfrac{d\bar{u}_{mod}}{dt}\left(\bar{t}_k\right)} \sum_{k=-\infty}^{\infty}\delta\left(t - D_s T_s - kT_s\right)\tilde{u}_{mod}(t) \tag{25}$$

According to *Property* 1, (25) is rewritten as

$$\tilde{\mathcal{P}}(s) = \mathcal{H}_{mod}\cdot\tilde{\mathcal{U}}_{mod}(s) \tag{26}$$

The HTF $\mathcal{H}_{mod}$ of the modulator is

$$\mathcal{H}_{mod} = F_m \begin{bmatrix} \ddots & \ddots & \ddots & \ddots & \ddots \\ \ddots & 1 & e^{j2\pi D_s} & e^{j4\pi D_s} & \ddots \\ \ddots & e^{-j2\pi D_s} & 1 & e^{j2\pi D_s} & \ddots \\ \ddots & e^{-j4\pi D_s} & e^{-j2\pi D_s} & 1 & \ddots \\ \ddots & \ddots & \ddots & \ddots & \ddots \end{bmatrix} \tag{27}$$

where

$$F_m = \frac{1}{V_{cm} - T_s \dfrac{d\bar{u}_{mod}}{dt}\left(\bar{t}_k\right)} \tag{28}$$

The spectra vectors are defined as

$$\tilde{\mathcal{P}}(s) = \left[\cdots, \tilde{p}\left(s-j\omega_s\right), \tilde{p}(s), \tilde{p}\left(s+j\omega_s\right), \cdots\right]^T \tag{29}$$

$$\tilde{\mathcal{U}}_{mod}(s) = \left[\cdots, \tilde{u}_{mod}\left(s-j\omega_s\right), \tilde{u}_{mod}(s), \tilde{u}_{mod}\left(s+j\omega_s\right), \cdots\right]^T \tag{30}$$

where $\omega_s=2\pi/T_s$, and others follow the same notation [25].

From (26), the following equations are established

$$\tilde{p}(s) = F_m \sum_{k=-\infty}^{\infty} e^{jk2\pi D_s}\tilde{u}_{mod}\left(s+jk\omega_s\right) \tag{31}$$

$$\tilde{p}\left(s+jn\omega_s\right) = e^{-jn2\pi D_s}\tilde{p}(s) \tag{32}$$

***Remark* 1**: In a DC-DC converter under analog control [19], the gain of feedback loops is expressed as

$$\tilde{u}_{mod}\left(s+jk\omega_s\right) = -T_c\left(s+jk\omega_s\right)\tilde{p}\left(s+jk\omega_s\right) \tag{33}$$

where $T_c(s)$ denotes the gain of the complete loop except for the modulator. By substituting (32) and (33) into (31), the SISO type transfer function of the modulator can be derived as

$$G_{PWM}(s) = \frac{\tilde{p}(s)}{\tilde{u}_{mod}(s)} = \frac{F_m}{1 + F_m \displaystyle\sum_{\substack{k\neq 0 \\ k=-\infty}}^{\infty} T_c\left(s+jk\omega_s\right)} \tag{34}$$

Clearly, the obtained result of $G_{PWM}(s)$ is consistent with [19]. Benefiting from the adoption of the HTF approach, the transfer function of the modulator is derived more concisely.

B. Sample-and-Hold Modeling

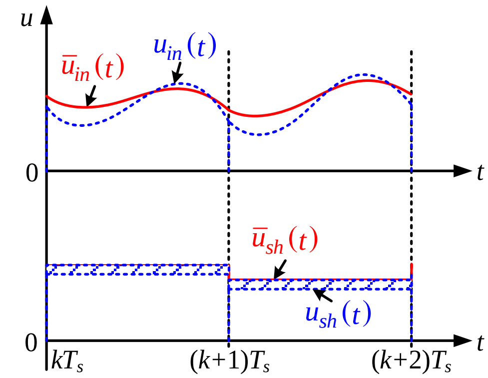

Fig. 2. Key waveforms of the sample-and-hold.

Besides the modulator, the sample-and-hold would also generate the sideband components in a digitally controlled system, whose key waveforms are shown in Fig. 2. $u_{in}(t)$ represents the continuous-time input, and $u_{sh}(t)$ is the discrete form of $u_{in}(t)$ by the sample-and-hold. The relationship between $u_{in}(t)$ and $u_{sh}(t)$ is expressed as

$$u_{sh}(t) = u_{in}\left(kT_s\right)\sum_{k=0}^{\infty}\left[\varepsilon\left(t-kT_s\right) - \varepsilon\left(t-(k+1)T_s\right)\right] \tag{35}$$

From (35), the sample-and-hold describes an LTP mapping relationship. Writing $u_{in}(kT_s)$ in an integral form gives

$$u_{in}\left(kT_s\right) = \int_{-\infty}^{\infty}\delta\left(\tau-kT_s\right)u_{in}(\tau)\,d\tau \tag{36}$$

A convolution expression is obtained by substituting (36) into (35)

$$u_{sh}(t) = \int_{-\infty}^{\infty} h_{sh}(t,\tau)u_{in}(\tau)\,d\tau \tag{37}$$

where

$$h_{sh}(t,\tau) = \sum_{k=0}^{\infty}\left[\varepsilon\left(t-kT_s\right) - \varepsilon\left(t-(k+1)T_s\right)\right]\delta\left(\tau-kT_s\right) \tag{38}$$

According to the definition, the time-periodic transfer function is calculated as

$$H_{sh}(t,s) = \sum_{k=0}^{\infty}\left[\varepsilon\left(t-kT_s\right) - \varepsilon\left(t-(k+1)T_s\right)\right]e^{-s\left(t-kT_s\right)} \tag{39}$$

Taking the Fourier transform to (39), the n_{th} Fourier coefficient of $H_{sh}(t, s)$ is derived as

$$H_{sh,n}(s) = \frac{1-e^{-\left(s+jn\omega_s\right)T_s}}{T_s\left(s+jn\omega_s\right)} \tag{40}$$

Therefore, the HTF of sample-and-hold is

$$\mathcal{H}_{sh}(s) = \frac{1}{T_s}\begin{bmatrix} \ddots & \vdots & \vdots & \vdots & ⋰ \\ \cdots & G_{zoh}\left(s-j\omega_s\right) & G_{zoh}\left(s-j\omega_s\right) & G_{zoh}\left(s-j\omega_s\right) & \cdots \\ \cdots & G_{zoh}(s) & G_{zoh}(s) & G_{zoh}(s) & \cdots \\ \cdots & G_{zoh}\left(s+j\omega_s\right) & G_{zoh}\left(s+j\omega_s\right) & G_{zoh}\left(s+j\omega_s\right) & \cdots \\ ⋰ & \vdots & \vdots & \vdots & \ddots \end{bmatrix} \tag{41}$$

where

$$G_{zoh}(s) = \frac{1-e^{-sT_s}}{s} \tag{42}$$

The following small-signal relationships can be found by $\mathcal{H}_{sh}(s)$ that

This article has been accepted for publication in a future issue of this journal, but has not been fully edited. Content may change prior to final publication. Citation information: DOI 10.1109/TIE.2021.3050389, IEEE Transactions on Industrial Electronics

$$\tilde{u}_{sh}(s)=\frac{G_{zoh}(s)}{T_s}\sum_{k=-\infty}^{\infty}\tilde{u}_{in}(s+jk\omega_s) \quad (43)$$

$$\tilde{u}_{sh}(s+jn\omega_s)=\frac{G_{zoh}(s+jn\omega_s)}{G_{zoh}(s)}\tilde{u}_{sh}(s) \quad (44)$$

C. Loop Gain Modeling

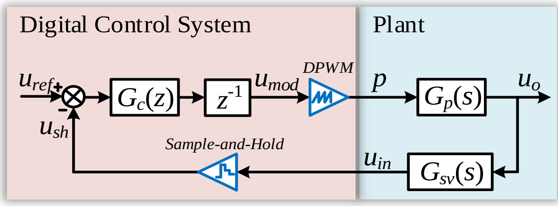

Fig. 3. Control block diagram of a digitally-controlled DC-DC converter.

The system diagram of a digitally controlled Buck converter with single loop feedback control is depicted in Fig. 3. $G_c(z)$ denotes the discrete-time digital controller, $G_p(s)$ and $G_{sv}(s)$ are the continuous transfer functions of controlled target and pre-ADC filter, respectively.

From Fig. 3, the mapping relationship from $\tilde{u}_{sh}(s)$ to $\tilde{u}_{mod}(s)$ is obtained as

$$\tilde{u}_{mod}(s)=-H_i'(s)\tilde{u}_{sh}(s) \quad (45)$$

where

$$H_i'(s)=\left[G_c(z)z^{-1}\right]\Big|_{z=e^{sT_s}} \quad (46)$$

In different frequency domains, (45) can be rewritten as

$$\tilde{u}_{mod}(s+jn\omega_s)=-H_i'(s+jn\omega_s)\tilde{u}_{sh}(s+jn\omega_s) \quad (47)$$

Based on (44), (45), and (47), $\tilde{u}_{mod}$ at different frequency domains satisfy

$$\tilde{u}_{mod}(s+jn\omega_s)=\frac{H_i(s+jn\omega_s)}{H_i(s)}\tilde{u}_{mod}(s) \quad (48)$$

where

$$H_i(s)=H_i'(s)G_{zoh}(s) \quad (49)$$

Due to the sample-and-hold effect in digital control, $\tilde{u}_{mod}(t)$ remains constant during one switching cycle, i.e.,

$$\frac{d\bar{u}_{mod}}{dt}(t_k)=0 \quad (50)$$

Based on (31), (48), and (50), the SISO type transfer function of Digital Pulse-Width Modulator (DPWM) is derived as

$$G_{DPWM}(s)=\frac{\tilde{p}(s)}{\tilde{u}_{mod}(s)}=\frac{1}{V_{cm}}\frac{S_i(s)}{H_i(s)} \quad (51)$$

where

$$S_i(s)=\sum_{k=-\infty}^{\infty}H_i(s+jk\omega_s)e^{jk2\pi D_s} \quad (52)$$

It is found that the exact transfer function of DPWM is equal to the multiplication of conventional average gain $1/V_{cm}$ and the complex gain $S_i(s)/H_i(s)$ determined by the digital control loop.

The SISO type transfer function of sample-and-hold can be deduced in a similar way. Inspection of Fig. 3 gives that

$$\tilde{u}_{in}(s)=H_o(s)\tilde{p}(s) \quad (53)$$

where

$$H_o(s)=G_{sv}(s)G_p(s) \quad (54)$$

Frequency shifting (53) at $s+jn\omega_s$ yields

$$\tilde{u}_{in}(s+jn\omega_s)=H_o(s+jn\omega_s)\tilde{p}(s+jn\omega_s) \quad (55)$$

According to (32), (53), and (55), it is derived that

$$\tilde{u}_{in}(s+jn\omega_s)=\frac{H_o(s+jn\omega_s)e^{-jn2\pi D_s}}{H_o(s)}\tilde{u}_{in}(s) \quad (56)$$

Putting (56) into (43) leads to

$$G_{S\&H}(s)=\frac{\tilde{u}_{sh}(s)}{\tilde{u}_{in}(s)}=\frac{G_{zoh}(s)}{T_s}\frac{S_o(s)}{H_o(s)} \quad (57)$$

where

$$S_o(s)=\sum_{k=-\infty}^{\infty}H_o(s+jk\omega_s)e^{-jk2\pi D_s} \quad (58)$$

The complex gain of sample-and-hold considering sideband effects is equal to the multiplication of conventional average gain $G_{zoh}(s)/T_s$ and the complex gain $S_o(s)/H_o(s)$ decided by the circuit dynamics.

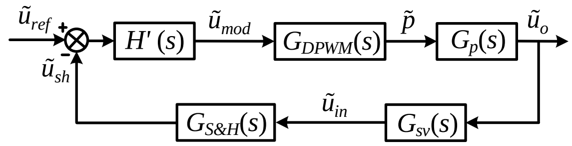

Fig. 4. Simplified small-signal structure of a digitally-controlled DC-DC converter.

Using (51) and (57), the block diagram of Fig. 3 can be simplified to Fig. 4. The whole system with the digital controller is represented in a continuous-time form rather than a discrete-time form.

The complete loop gain expression is given by

$$T(s)=\frac{1}{V_{cm}T_s}S_i(s)S_o(s) \quad (59)$$

which includes two infinite series introduced by DPWM and sample-and-hold. While in the conventional average model, the loop gain is

$$T_{avg}(s)=\frac{1}{V_{cm}T_s}H_i(s)H_o(s) \quad (60)$$

It is shown that the transfer function $H_i(s)$ and $H_o(s)$ will be extended to the infinite series $S_i(s)$ and $S_o(s)$ when the sideband effects are taken into consideration.

D. Loop Gain Measurement

The loop gain of a given closed-loop system provides essential information for stability assessment [32]-[34]. In the digitally controlled systems, it has been observed that different perturbation injection points lead to different measurement results of the loop gain [21]-[22]. However, the reason for the measurement discrepancy has not been explained so far [23]. There are two main reasons which hamper the analysis of loop gain measurement in digitally controlled systems. On one hand, the sample-and-hold in digital control brings an extra time-periodic link. On the other hand, due to the intrinsic continuous-time nature of measuring equipment, continuous dynamics of the system should be preserved in the model, which is abandoned by the discrete-time model.

The perturbation can be injected into the loop through (I) the sampling path or (II) the modulation path, as shown in Fig. 5. A sample-and-hold exists in case (II) due to digital control.

This article has been accepted for publication in a future issue of this journal, but has not been fully edited. Content may change prior to final publication. Citation information: DOI 10.1109/TIE.2021.3050389, IEEE Transactions on Industrial Electronics

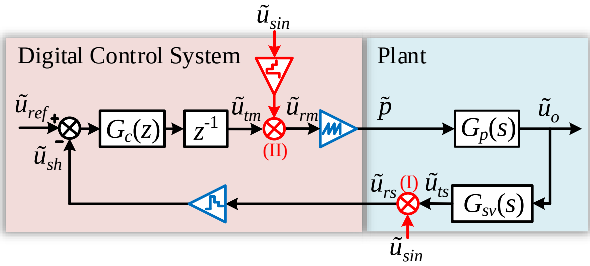

Fig. 5. Different perturbation schemes of a digitally-controlled system.

When the perturbation is injected into (I), according to *Property* 1 and *Property* 2, the harmonic transfer function from $\tilde{u}_{rs}$ to $\tilde{u}_{ts}$ is deduced as

$$\tilde{\mathcal{U}}_{ts}(s) = -\mathcal{H}_o(s)\mathcal{H}_{mod}\mathcal{H}_i'(s)\mathcal{H}_{sh}(s)\cdot\mathcal{H}_{rs}(s) \tag{61}$$

where

$$\mathcal{H}_i'(s) = \begin{bmatrix} \ddots & \ddots & \ddots & \ddots & \ddots \\ \ddots & H_i'(s-j\omega_s) & 0 & 0 & \ddots \\ \ddots & 0 & H_i'(s) & 0 & \ddots \\ \ddots & 0 & 0 & H_i'(s+j\omega_s) & \ddots \\ \ddots & \ddots & \ddots & \ddots & \ddots \end{bmatrix} \tag{62.a}$$

$$\mathcal{H}_o(s) = \begin{bmatrix} \ddots & \ddots & \ddots & \ddots & \ddots \\ \ddots & H_o(s-j\omega_s) & 0 & 0 & \ddots \\ \ddots & 0 & H_o(s) & 0 & \ddots \\ \ddots & 0 & 0 & H_o(s+j\omega_s) & \ddots \\ \ddots & \ddots & \ddots & \ddots & \ddots \end{bmatrix} \tag{62.b}$$

By solving (61), it is derived that

$$\tilde{u}_{ts}(s+jn\omega_s) = -\frac{H_o(s+jn\omega_s)e^{-j2n\pi D_s}}{V_{cm}T_s}S_i(s)\sum_{m=-\infty}^{\infty}\tilde{u}_{rs}(s+jm\omega_s) \tag{63}$$

which implies that

$$\tilde{u}_{ts}(s+jn\omega_s) = \frac{H_o(s+jn\omega_s)e^{-j2n\pi D_s}}{H_o(s)}\tilde{u}_{ts}(s) \tag{64}$$

From Fig. 5, the following relationships hold

$$\begin{cases} \tilde{u}_{rs}(s) = \tilde{u}_{ts}(s) + \tilde{u}_{sin}(s) \\ \tilde{u}_{rs}(s+jn\omega_s) = \tilde{u}_{ts}(s+jn\omega_s) \end{cases}, (n \in \mathbb{Z}\setminus 0) \tag{65}$$

According to (63)-(65), it is deduced that

$$\frac{\tilde{u}_{ts}(s)}{\tilde{u}_{sin}(s)} = -\frac{S_i(s)H_o(s)}{V_{cm}T_s\left[1+T(s)\right]} \tag{66}$$

$$T_{\mathrm{I}}(s) = -\frac{\tilde{u}_{ts}(s)}{\tilde{u}_{rs}(s)} = \frac{S_i(s)H_o(s)}{V_{cm}T_s\left[1+T(s)\right]-S_i(s)H_o(s)} \tag{67}$$

It is found that $T_{\mathrm{I}}(s)$ is equal to $T(s)$ if $H_o(s)=S_o(s)$ which means that this measurement scheme is applicable under small switching ripples.

Similarly, the corresponding results of injecting perturbation into the point (II) can be obtained as

$$\frac{\tilde{u}_{tm}(s)}{\tilde{u}_{sin}(s)} = -\frac{S_o(s)H_i(s)S_{zoh}(s)}{V_{cm}T_s\left[1+T(s)\right]} \tag{68}$$

and (69) shown at the bottom of the page. The $S_{zoh}(s)$ is represented as

$$S_{zoh}(s) = \sum_{m=-\infty}^{\infty} G_{zoh}(s+jm\omega_s)e^{j2m\pi D_s} \tag{70}$$

When $S_i(s)G_{zoh}(s)=H_i(s)S_{zoh}(s)$ is satisfied, the measured $T_{\mathrm{II}}(s)$ is equal to $T(s)$.

***Remark* 2**: In the sense of average modeling (i.e., the sideband effects are neglected), $S_i(s)=H_i(s)$ and $S_o(s)=H_o(s)$ hold. Thus, it is traditionally considered that loop gain measurement is independent of the injection points in the digitally controlled system with single loop feedback control. However, when considering sideband effects, it is found that $T_{\mathrm{I}}(s)$ is not the same as $T_{\mathrm{II}}(s)$, which implies that the measured loop gain depends on the locations of information injection. Moreover, $T_{\mathrm{I}}(s)$ and $T_{\mathrm{II}}(s)$ are not directly equal to the real loop gain $T(s)$. And only under certain conditions can the right loop gain be measured.

E. Discussion

According to the definition, the loop gain is the product of the gains around the forward and feedback paths of the loop at the same frequency [32]. In this paper, the derivation of the loop gain $T(s)$ follows strictly the definition. Compared with the loop gain $T_{avg}(s)$ in the average sense, the main difference is that the modulator model and the sample-and-hold model in the accurate loop gain take into account the sideband effect. Under the proposed modeling framework, the modulator model $G_{DPWM}(s)$ depends on the equivalent digital control transfer function $H_i(s)$ while the sample-and-hold model $G_{S\&H}(s)$ is influenced by the equivalent plant transfer function $H_o(s)$. This coupling phenomenon results from the time-periodic dynamics, which cannot be reflected by the average model.

Moreover, as observed from (66) and (68), the stability of closed-loop response to disturbance is determined by $1+T(s)$. Therefore, the calculated loop gain $T(s)$ can be used for stability assessment. In summary, the loop gain $T(s)$ with capturing the sideband effect can be regarded as the generalized loop gain.

IV. Analytical Continuous-Time Model Derivation of Digitally Controlled Buck System

In (59), two infinite series are contained in the loop gain, which makes it inconvenient to apply in practical analysis. Two basic formulas for calculating the sum of infinite series are given as follows.

***Lemma* 1**: For given constant ω_x and D, in which D is a real number with $D\in(0,1)$. Then, the following relationship holds

$$\sum_{n=-\infty}^{\infty}\frac{e^{jn2\pi D}}{s+jn\omega_x} = \frac{2\pi}{\omega_x}\frac{e^{-2D\pi s/\omega_x}e^{\pi s/\omega_x}}{e^{\pi s/\omega_x}-e^{-\pi s/\omega_x}} \tag{71}$$

Proof of ***Lemma* 1** is given in the Appendix.

***Lemma* 2**: For given constant γ, ω_x, and D, in which the real-part of γ is greater than zero and D is a real number with $D\in(0,1)$. Then, the following relationship holds

$$\sum_{n=-\infty}^{\infty}\frac{e^{-jn2\pi D}}{s+\gamma+jn\omega_x} = \frac{2\pi}{\omega_s}\frac{e^{2D\pi(s+\gamma)/\omega_x}e^{-\pi(s+\gamma)/\omega_x}}{e^{\pi(s+\gamma)/\omega_x}-e^{-\pi(s+\gamma)/\omega_x}} \tag{72}$$

Proof of ***Lemma* 2** is given in the Appendix.

$$T_{\mathrm{II}}(s) = -\frac{\tilde{u}_{tm}(s)}{\tilde{u}_{rm}(s)} = \frac{S_o(s)H_i(s)S_{zoh}(s)}{V_{cm}T_sG_{zoh}(s)\left[1+T(s)\right]-S_o(s)H_i(s)S_{zoh}(s)} \tag{69}$$

This article has been accepted for publication in a future issue of this journal, but has not been fully edited. Content may change prior to final publication. Citation information: DOI 10.1109/TIE.2021.3050389, IEEE Transactions on Industrial Electronics

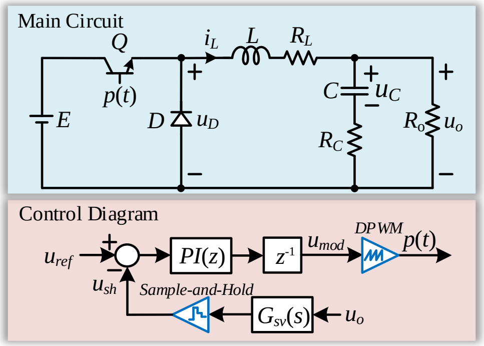

Fig. 6. Circuit diagram of digitally-controlled Buck converter.

A. Analytical Form of the Loop Gain Model

In order to illustrate this modeling method clearly, a digitally controlled Buck converter depicted in Fig. 6 is taken for example. This circuit diagram is composed of the main circuit, the digital controller, the sample-and-hold, and the digital pulse-width modulator. In the main circuit, Q is an active switch, D is a diode, R_o is the load resistor, L is the inductor in series with the resistor R_L, C is the output filter capacitor, R_C is the Equivalent Series Resistor (ESR) of the output capacitor, E is the input DC voltage and u_o is the output voltage. i_L and u_C denote the inductor current and capacitor voltage, respectively.

According to Fig. 6, the transfer function of the PI controller in the z-domain is

$$G_c(z) = k_p + \frac{k_i T_s}{1 - z^{-1}} \tag{73}$$

Then, (49) can be expressed as

$$H_i(s) = \frac{e^{-sT_s}}{s}\left[k_p\left(1 - e^{-sT_s}\right) + k_i T_s\right] \tag{74}$$

where k_p and k_i are the proportional gain and integral gain of the PI controller, respectively.

The infinite series $S_i(s)$ can then be described as

$$S_i(s) = e^{-sT_s}\left[k_p\left(1 - e^{-sT_s}\right) + k_i T_s\right]\sum_{m=-\infty}^{\infty}\frac{e^{jm2\pi D_s}}{s + jm\omega_s} \tag{75}$$

Applying *Lemma* 1 to (75) yields

$$S_i(s) = e^{-sT_s}\left[\left(1 - e^{-sT_s}\right)k_p + k_i T_s\right]\frac{2\pi}{\omega_s}\frac{e^{-2D_s\pi s/\omega_s}e^{\pi s/\omega_s}}{e^{\pi s/\omega_s} - e^{-\pi s/\omega_s}} \tag{76}$$

In the main circuit, the sampling delay is modeled as

$$G_{sv}(s) = \frac{\omega_{sam}}{s + \omega_{sam}} \tag{77}$$

where ω_{sam} is the cutoff frequency of the anti-aliasing filter for voltage measurement. And the transfer function $G_p(s)$ from pulse trains p to output voltage u_o is represented in (78) shown at the bottom of the page. Then the factorization form of $H_o(s)$ is provided as

$$H_o(s) = \sum_{k=1}^{3}\frac{A_k}{s + \gamma_k} \tag{79}$$

where

$$A_1 = \omega_{sam} E R_o\left(1 - CR_C\gamma_1\right)\Big/\left[a\left(\gamma_2 - \gamma_1\right)\left(\gamma_3 - \gamma_1\right)\right] \tag{80.a}$$

$$A_2 = \omega_{sam} E R_o\left(1 - CR_C\gamma_2\right)\Big/\left[a\left(\gamma_1 - \gamma_2\right)\left(\gamma_3 - \gamma_2\right)\right] \tag{80.b}$$

$$A_3 = \omega_{sam} E R_o\left(1 - CR_C\gamma_3\right)\Big/\left[a\left(\gamma_1 - \gamma_3\right)\left(\gamma_2 - \gamma_3\right)\right] \tag{80.c}$$

$$\gamma_1 = \omega_{sam} \tag{80.d}$$

$$\gamma_2 = -\left(-b + \sqrt{b^2 - 4ac}\right)\Big/(2a) \tag{80.e}$$

$$\gamma_3 = -\left(-b - \sqrt{b^2 - 4ac}\right)\Big/(2a) \tag{80.f}$$

$$a = LC\left(R_C + R_o\right) \tag{80.g}$$

$$b = L + CR_L\left(R_C + R_o\right) + CR_o R_C \tag{80.h}$$

$$c = R_L + R_o \tag{80.i}$$

Similarly, according to *Lemma* 2, the following infinite series sum is given as

$$S_o(s) = \sum_{k=1}^{3}\frac{2\pi A_k}{\omega_s}\frac{e^{2D_s\pi(s+\gamma_k)/\omega_s}e^{-\pi(s+\gamma_k)/\omega_s}}{e^{\pi(s+\gamma_k)/\omega_s} - e^{-\pi(s+\gamma_k)/\omega_s}} \tag{81}$$

Based on the calculations above, it is found that the poles of $T(s)$ are $0\pm jn\omega_s$ and $-\gamma_k\pm jn\omega_s$ (n=0, ±1, ±2, …), which are the translated copies of $T_{avg}(s)$ with shifting proportional to the switching angular frequency ω_s. This means that the number of Right-Half Plane (RHP) poles of $T(s)$ can be easily determined by $T_{avg}(s)$. And substituting (76) and (81) into (59), the analytical expression of loop gain can be obtained.

B. Controller Design Method

In order to introduce the reader to a few possible applications of the proposed model in controller parameter design, a brief example is given as follows.

Suppose ω_c is the cutoff angular frequency and PM/deg is the phase margin of the system. Then, it gives

$$T\left(j\omega_c\right) = -e^{j\frac{PM}{180}\pi} \tag{82}$$

By separating the real part and imaginary part of (82), the expressions of k_p and k_i are derived as

$$k_p = \frac{m_1\mu_3 + m_2\mu_1}{\mu_4\mu_1 - \mu_2\mu_3} \tag{83}$$

$$k_i = \frac{m_2\left(\mu_1 - \mu_2\right) - m_1\left(\mu_4 - \mu_3\right)}{\left(\mu_2\mu_3 - \mu_4\mu_1\right)T_s} \tag{84}$$

where

$$m_1 = \frac{2V_{cm}}{T_s}\sin\left(\pi\frac{\omega_c}{\omega_s}\right)\cos\left(\frac{PM - 90}{180}\pi + \omega_c T_s\right) \tag{85.a}$$

$$m_2 = \frac{2V_{cm}}{T_s}\sin\left(\pi\frac{\omega_c}{\omega_s}\right)\sin\left(\frac{PM - 90}{180}\pi + \omega_c T_s\right) \tag{85.b}$$

$$\mu_1 = \sum_{k=1}^{3}\chi_k\left(e^{\pi\frac{\gamma_k}{\omega_s}} - e^{-\pi\frac{\gamma_k}{\omega_s}}\right)\cos\left(\pi\frac{\omega_c}{\omega_s}\right) \tag{85.c}$$

$$\mu_2 = \sum_{k=1}^{3}\chi_k\left[e^{\pi\frac{\gamma_k}{\omega_s}}\cos\left(\pi\frac{\omega_c}{\omega_s} + \omega_c T_s\right) - e^{-\pi\frac{\gamma_k}{\omega_s}}\cos\left(\pi\frac{\omega_c}{\omega_s} - \omega_c T_s\right)\right] \tag{85.d}$$

$$G_p(s) = \frac{ER_o\left(CR_C s + 1\right)}{LC\left(R_C + R_o\right)s^2 + \left[L + CR_L\left(R_C + R_o\right) + R_o CR_C\right]s + \left(R_L + R_o\right)} \tag{78}$$

This article has been accepted for publication in a future issue of this journal, but has not been fully edited. Content may change prior to final publication. Citation information: DOI 10.1109/TIE.2021.3050389, IEEE Transactions on Industrial Electronics

TABLE II
COMPARISON OF THE EXISTING SMALL-SIGNAL MODELS AND THE PROPOSED MODELS FOR BUCK CONVERTERS

	Two-frequency model[15]-[16]	Four-frequency model[17]	Matrix-Based multi-frequency model[18]	Extended-frequency model[19]	Generalized multi-frequency model[20]	Proposed model
Control mode	Analog	Analog	Analog	Analog	Analog	Digital
Time-periodic components	Modulator	Modulator	Modulator	Modulator	Modulator	Modulator Sample-and-hold
Sideband frequencies	ω-ω_s	ω-ω_s ω+ω_s	All	All	ω-ω_s ω+ω_s or ω-2ω_s	All
Steady-state operating points	DC	DC First-order harmonic	DC	All	DC First-order harmonic	All
Model form	SISO	SISO	MIMO	SISO	SISO/MIMO	SISO/MIMO
Analyticity	Good	Good	Good	Medium	Good	Good

TABLE I
PARAMETERS OF THE BUCK SYSTEM

Symbol	Description	Value
E	Input voltage	50 V
R_o	Load resistance	5 Ω
L	Inductance	0.5 mH
R_L	Inductor resistance	0.3 Ω
C	Output capacitance	20 μF
R_C	Capacitor ESR	0.003 Ω
V_{cm}	Amplitude of carrier signal	50 V
ω_{sam}	ADC cutoff frequency	$47.4\times10^3\pi$ rad/s
f_s	Switching frequency	5 kHz
f_{sam}	Sampling frequency	5 kHz

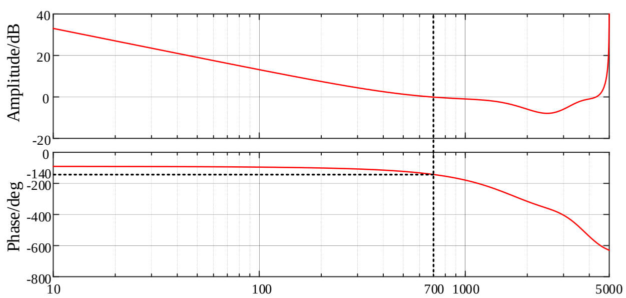

Fig. 7. Bode diagrams of the loop gain with calculated controller parameters.

$$\mu_3=\sum_{k=1}^{3}\chi_k\left(e^{\pi\frac{\gamma_k}{\omega_s}}+e^{-\pi\frac{\gamma_k}{\omega_s}}\right)\sin\left(\pi\frac{\omega_c}{\omega_s}\right) \tag{85.e}$$

$$\mu_4=\sum_{k=1}^{3}\chi_k\left[e^{\pi\frac{\gamma_k}{\omega_s}}\sin\left(\pi\frac{\omega_c}{\omega_s}+\omega_c T_s\right)+e^{-\pi\frac{\gamma_k}{\omega_s}}\sin\left(\pi\frac{\omega_c}{\omega_s}-\omega_c T_s\right)\right] \tag{85.f}$$

$$\chi_k=\frac{A_k e^{\gamma_k\left(D_s-\frac{1}{2}\right)T_s}}{e^{2\pi\frac{\gamma_k}{\omega_s}}+e^{-2\pi\frac{\gamma_k}{\omega_s}}-2\cos\left(2\pi\frac{\omega_c}{\omega_s}\right)} \tag{85.g}$$

The main parameters are given in Table I. Choosing ω_c=1400π rad/s and PM=40°, the controller parameters are calculated as k_p=0.3835 and k_i=2531 with the steady-state duty ratio D_s=0.5. The calculated controller parameters are used in this paper. The Bode diagram under the calculated controller parameters is plotted as Fig. 7. As observed, the controller meets the design objectives, providing the validity of the proposed model in the controller parameter design.

C. Influence of Sideband Effects on Loop Gain

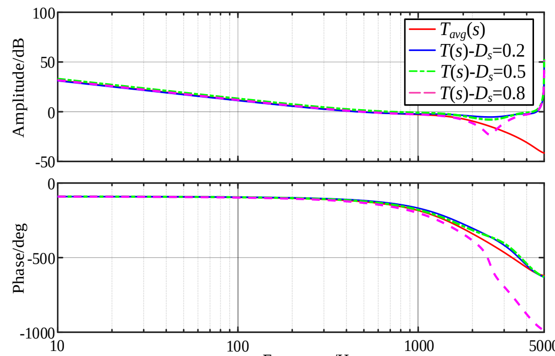

Fig. 8. Bode diagrams of the loop gain with different D_s.

The focus of this paper is to reveal the unknown phenomena in loop gain measurement; thus, the system parameters are purposely chosen to introduce substantial ripple components so as to maximally demanding on the prediction model. Moreover, in high-power applications, the selected low switching frequency is reasonable due to the constraint of efficiency or power devices.

As shown in Fig. 8, the loop gain derived from the average model is basically the same as the exact model in the regions of frequencies below f_s/5. The amplitude gain of $T(s)$ is symmetrical with respect to f=f_s/2, which conforms to the aliasing effect in the digitally controlled systems [31]. The symmetry results in the cutoff frequencies to occur in pairs. And the phase derived by $T(s)$ may be either lead or lag the phase estimated by the average model.

Applying *Lemma* 1 to (70), the $S_{zoh}(s)$ is solved as

$$S_{zoh}(s)=\left(1-e^{-sT_s}\right)\frac{2\pi}{\omega_s}\frac{e^{-2D_s\pi s/\omega_s}e^{\pi s/\omega_s}}{e^{\pi s/\omega_s}-e^{-\pi s/\omega_s}} \tag{86}$$

Based on the above calculations, it is found that $S_i(s)G_{zoh}(s)$=$H_i(s)S_{zoh}(s)$ is established, which implies that $T_{\text{II}}(s)$ is equal to the exact loop gain $T(s)$. While injecting into the sampling path, the measured result $T_{\text{I}}(s)$ is not the real loop gain $T(s)$ because of $H_o(s)\neq S_o(s)$.

This article has been accepted for publication in a future issue of this journal, but has not been fully edited. Content may change prior to final publication. Citation information: DOI 10.1109/TIE.2021.3050389, IEEE Transactions on Industrial Electronics

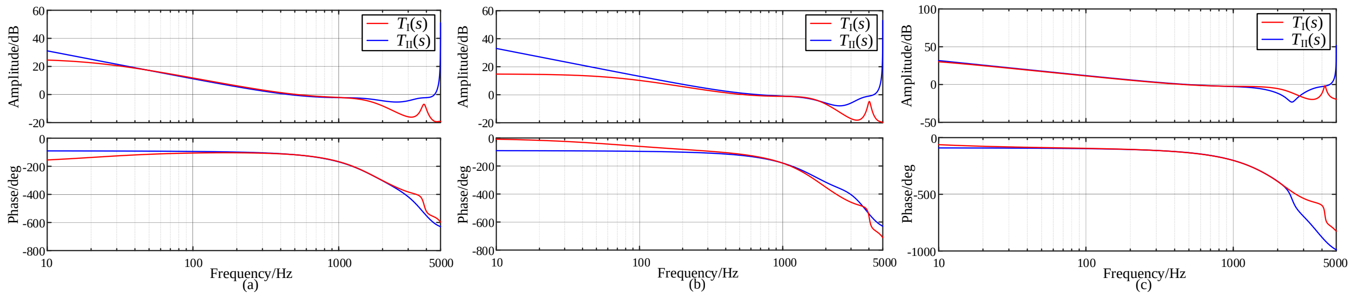

Fig. 9. Bode diagrams of $T_{\mathrm{I}}(s)$ and $T_{\mathrm{II}}(s)$ with different D_s. (a) D_s=0.2; (b) D_s=0.5; (c) D_s=0.8.

Fig. 9 gives the Bode diagram of $T_{\mathrm{I}}(s)$ and $T_{\mathrm{II}}(s)$ with different D_s. $T_{\mathrm{I}}(s)$ matches well with $T_{\mathrm{II}}(s)$ only in the middle frequency regions, indicating that the information injection point plays an important role in the measured result. And the deviation between these two measurement schemes is related to the steady-state duty cycle D_s. Based on the discussions before, the loop gain measurement by perturbing the sampling signal is failed to obtain the real loop gain.

D. Comparison Between the Existing Small-Signal Models and the Proposed Analytical Model

Table II summarizes the comparison results of the existing small-signal models and the proposed model. As shown in Table II, existing studies are mostly focused on modeling Buck converters under analog control, where only the PWM produces the sideband effects [15]-[20]. In digitally controlled systems, the sample-and-hold also results in sideband effects, which complicates the system model. Up to now, no accurate continuous-time small-signal model of digitally controlled Buck converters has been presented for sideband effects analysis.

On the other hand, the two-frequency model, four-frequency model, and the generalized multi-frequency model do improve the model accuracy by considering a finite number of sideband components, but the accuracy of these models is verified from a practical rather than a theoretical perspective. The matrix-based multi-frequency model does not consider the ripple gradient in the modulation signal, which may be a potential limitation for model accuracy. The extended-frequency model achieves extremely high accuracy, but the lack of analytical form makes it inconvenient in practical analysis. The proposed model has an analytical form while considering all the sideband components; thus, it is a promising choice for sideband effects analysis.

V. Experimental Verification

In this section, a prototype of the digitally controlled Buck converter is built to verify the correctness of the proposed models, as shown in Fig. 10. In the prototype, the used active switch is IRFP140PBF (100 V/31 A, Vishay) and the diode is FEP30BP (100 V/30 A, Vishay). The system specifications are the same as the simulation parameters in Table I. The control platform is based on a floating-point Digital Signal Processor (DSP) TMS320F28335. The injected small perturbation from 10 Hz to 5 kHz is generated by Agitek ATA-122D Wide Band Amplifier with an isolation transformer. And the measured signals are sent to the frequency response analyzer Bode 100.

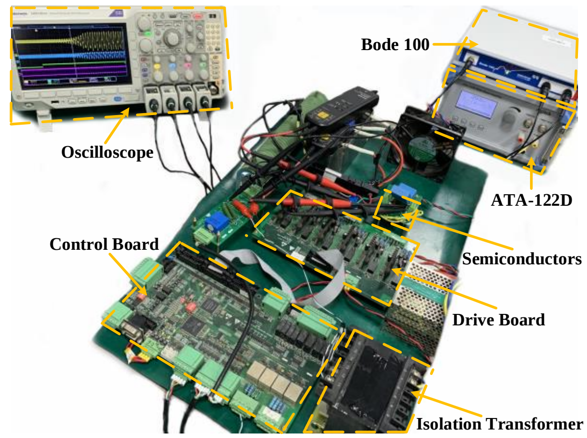

Fig. 10. Experimental setup for loop gain measurement verification.

The implementations of the two measurement schemes are illustrated in Fig. 11. The measured loop gain is obtained by plotting the Bode diagram of -*Test*/*Ref*. In the sampling path perturbation scheme, the sampled output voltage of DSP is the sum of perturbation and the actual capacitor voltage. The actual capacitor voltage is the returned signal sending into the *Test* port, while the sampled output voltage is the feedforward signal to the *Ref* port. In the modulation path perturbation scheme, the perturbed modulation signal consists of the actual modulation signal and perturbation. The perturbed modulation signal sends to the *Ref* port, and the actual modulation signal transmits to the *Test* port.

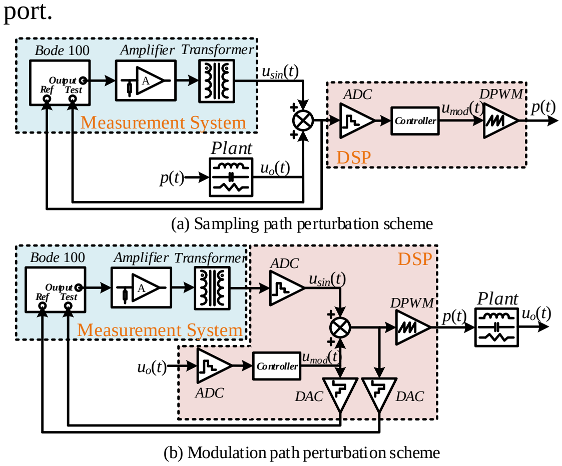

Fig. 11. Implementation diagram of loop gain measurement scheme.

This article has been accepted for publication in a future issue of this journal, but has not been fully edited. Content may change prior to final publication. Citation information: DOI 10.1109/TIE.2021.3050389, IEEE Transactions on Industrial Electronics

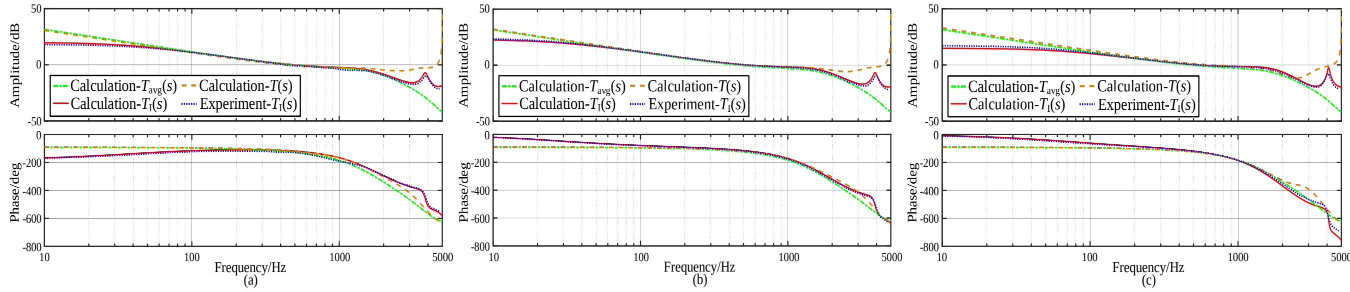

Fig. 12. Bode diagrams of the calculated and measured $T_I(s)$ together with $T_{avg}(s)$ and $T(s)$. (a) u_{ref}=10 V; (b) u_{ref}=20 V; (c) u_{ref}=30 V.

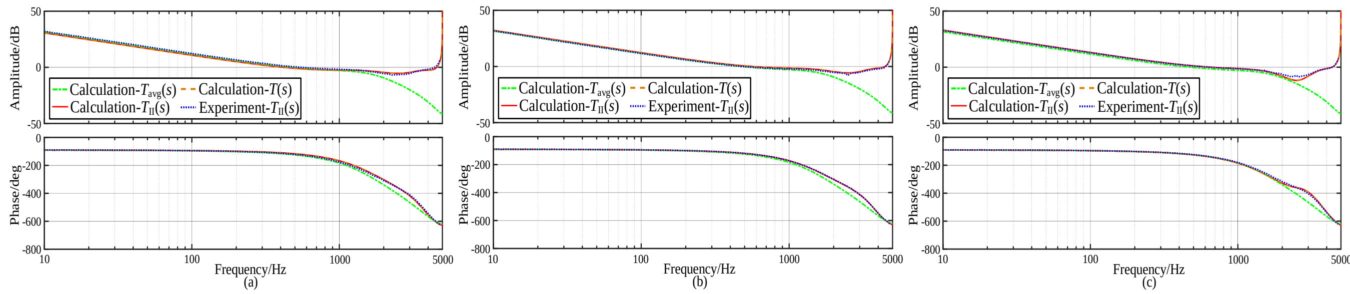

Fig. 13. Bode diagrams of the calculated and measured $T_{II}(s)$ together with $T_{avg}(s)$ and $T(s)$. (a) u_{ref}=10 V; (b) u_{ref}=20 V; (c) u_{ref}=30 V.

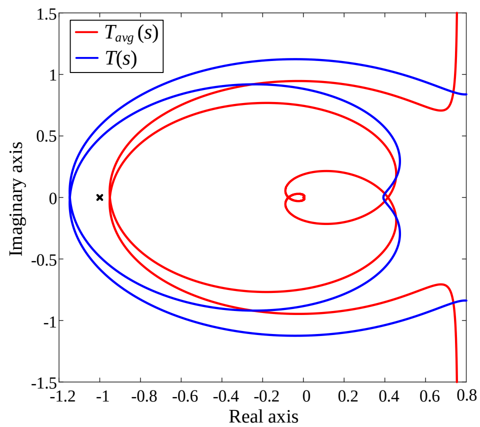

Fig. 14. Nyquist plots of the loop gains calculated by different models.

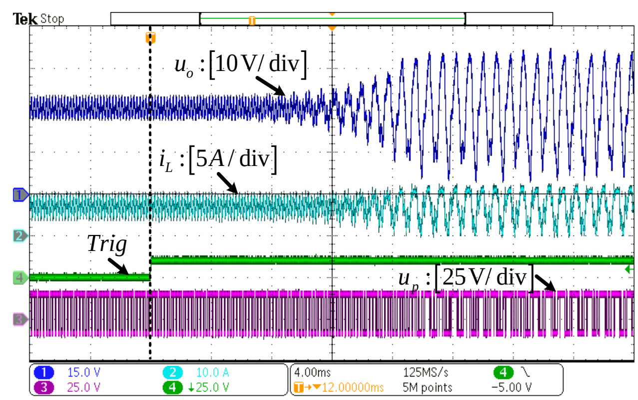

Fig. 15. Experimental waveforms of output voltage u_o, inductor current i_L and drive voltage u_p with a sudden change of control parameters.

When the point of information injection is placed on the sampling path, the calculated and measured Bode diagrams of $T_I(s)$ with different output voltage references u_{ref} are shown in Fig. 12. Similarly, the calculated responses and measured responses of $T_{II}(s)$ are plotted as shown in Fig. 13. As seen, all the measured responses are matched well with the calculated responses up to the switching frequency, which verifies the validity of the developed small-signal continuous-time model of digitally controlled Buck system. And the frequency responses are different along with different steady-state operating points.

Clearly, the frequency responses of $T_I(s)$ are not the same as $T_{II}(s)$, which demonstrates that the measured loop gain is dependent on the point of injection even with the simplest single loop feedback control. From Fig. 12, $T_I(s)$ resembles the actual loop gain $T(s)$ only in the middle frequency regions. From Fig. 13, $T_{II}(s)$ is in accord well with $T(s)$. The fact gives the conclusion that the right loop gain can be measured when the injection point is in the modulation path but the sampling path perturbation scheme fails to do that. Moreover, the average loop gain $T_{avg}(s)$ is close to the actual loop gain $T(s)$ in the low-frequency regions, but the deviation enlarges as the frequency of interest increases.

As discussed before, no RHP pole exists in $T(s)$. Therefore, Nyquist criterion is adopted here for stability prediction rather than Bode diagram criterion due to the presence of multiple cutoff frequencies. When u_{ref}=30 V, the Nyquist plots of $T(s)$ and $T_{avg}(s)$ with k_p=0.9273 and k_i=400.9 are shown in Fig. 14. The blue Nyquist curve encircles the critical point (-1, j0), which means that the system is unstable. In contrast, the system is predicted to be stable by the average model. In Fig. 15, the experimental waveforms of the converter under this case are presented. When the signal *Trig* represented by the green line steps into a high level, the controller parameters are changed to k_p=0.9273 and k_i=400.9. As a result, both the output voltage u_o and inductor current i_L begin to fluctuate. Finally, the system exhibits unstable phenomena in steady-state, verifying the credibility of the proposed model in offering accurate stability information. It is worth noting that this instability cannot be predicted by the conventional average model.

VI. Conclusion

An accurate small-signal continuous-time model of digitally controlled Buck system operating in continuous-conduction mode under constant-frequency voltage-mode control is developed and experimentally verified. All the sideband components ($\omega\pm k\omega_s$, $k\in\mathbb{Z}$) introduced by the PWM and the sample-and-hold are explicitly incorporated into the small-signal model. No approximation was made in the modeling process so that the model is completely accurate in the full frequency domain, which breaks the limit of Nyquist frequency. Also, the analytical form of the loop gain expression, which consists of two infinite series, was derived.

On the other hand, a quantitative relation between the measured loop gain and the location of the injection point can be derived, by using the harmonic transfer function model. It has been theoretically proved and experimentally verified that the modulation path perturbation scheme and the sampling path perturbation scheme lead to different loop gain measurement results. The measurement results of different perturbation schemes only match well in the area around the cutoff frequency. Besides, the conditions that the measured loop gain is the actual loop gain are given.

The proposed small-signal model can be generalized to the case of the double-edge modulator. A detailed analysis of the influence of different modulation strategies on system stability in different digitally controlled DC/DC converters will be the topic of a follow-up paper.

APPENDIX

PROOF OF LEMMA 1

Choose $\alpha\notin\mathbb{Z}$ and define a function with a period of 2π

$$f_T(t)=\cos(\alpha t),-\pi<t<\pi \tag{A1}$$

Applying Fourier transform to $f_T(t)$, the Fourier coefficients (n=0, 1, 2, …) are

$$a_n=\frac{1}{\pi}\int_{-\pi}^{\pi}f_T(t)\cos(nt)\,dt=(-1)^n\frac{2\alpha\sin(\alpha\pi)}{\pi(\alpha^2-n^2)} \tag{A2}$$

$$b_n=\frac{1}{\pi}\int_{-\pi}^{\pi}f_T(t)\sin(nt)\,dt=0 \tag{A3}$$

Then, $f_T(t)$ can be represented as

$$\cos(\alpha t)=\frac{\sin\alpha\pi}{\pi}\left[\frac{1}{\alpha}+\sum_{n=1}^{\infty}(-1)^n\frac{2\alpha}{\alpha^2-n^2}\cos nt\right] \tag{A4}$$

Selecting $t=\pi$ yields

$$\cos(\alpha\pi)=\frac{\sin(\alpha\pi)}{\pi}\left(\frac{1}{\alpha}+\sum_{n=1}^{\infty}\frac{2\alpha}{\alpha^2-n^2}\right) \tag{A5}$$

Therefore, the following equation is established

$$\pi\cot(\alpha\pi)=\sum_{n=-\infty}^{\infty}\frac{1}{\alpha+n} \tag{A6}$$

Choose $x\in\mathbb{R}\cap(0,2\pi)$ and define two sum functions

$$S_K(x)=\sum_{n=-K}^{K}\frac{\sin[(n+\alpha)x]}{n+\alpha} \tag{A7}$$

$$P_K(x)=\sum_{n=-K}^{K}\frac{\cos[(n+\alpha)x]}{n+\alpha} \tag{A8}$$

Taking the derivatives of (A7) and (A8) yield

$$S_K'(x)=\sum_{n=-K}^{K}\cos[(n+\alpha)x] \tag{A9}$$

$$P_K'(x)=-\sum_{n=-K}^{K}\sin[(n+\alpha)x] \tag{A10}$$

Based on the following relationships

$$\cos[(n+\alpha)x]=\frac{\sin\left[\left(n+\alpha+\frac{1}{2}\right)x\right]-\sin\left[\left(n+\alpha-\frac{1}{2}\right)x\right]}{2\sin\left(\frac{x}{2}\right)} \tag{A11}$$

$$\sin[(n+\alpha)x]=\frac{\cos\left[\left(n+\alpha+\frac{1}{2}\right)x\right]-\cos\left[\left(n+\alpha-\frac{1}{2}\right)x\right]}{-2\sin\left(\frac{x}{2}\right)} \tag{A12}$$

(A9) and (A10) can be rewritten as

$$S_K'(x)=\cos(\alpha x)\left[\cos(Kx)+\frac{\sin(Kx)\cos\left(\frac{x}{2}\right)}{\sin\left(\frac{x}{2}\right)}\right] \tag{A13}$$

$$P_K'(x)=-\sin(\alpha x)\left[\cos(Kx)+\frac{\sin(Kx)\cos\left(\frac{x}{2}\right)}{\sin\left(\frac{x}{2}\right)}\right] \tag{A14}$$

According to Riemann-Lebesgue Lemma [35], it is derived that

$$\lim_{K\to\infty}S_K'(x)=0 \tag{A15}$$

$$\lim_{K\to\infty}P_K'(x)=0 \tag{A16}$$

which implies that $S_\infty(x)$ and $P_\infty(x)$ are constants.

Selecting x=1 and K=∞ yields

$$S_\infty(1)=\sum_{n=-\infty}^{\infty}\frac{\sin(n+\alpha)}{n+\alpha} \tag{A17}$$

Define a function $\chi_1(t)\in L^1_{[-\pi,\pi]}$ with a period of 2π

$$\chi_1(t)=\begin{cases}e^{-j\alpha t}, |t|<1\\ 0, otherwise\end{cases} \tag{A18}$$

The Fourier coefficients of $\chi_1(t)$ are deduced as

$$\hat{\chi}_1(n)=\frac{1}{2\pi}\int_{-\pi}^{\pi}\chi_1(t)e^{-jnt}dt=\frac{1}{\pi}\frac{\sin(n+\alpha)}{n+\alpha} \tag{A19}$$

Therefore, $\chi_1(t)$ can be represented as

$$\chi_1(t)=\sum_{n=-\infty}^{\infty}\frac{1}{\pi}\frac{\sin(n+\alpha)}{n+\alpha}e^{jnt} \tag{A20}$$

Choosing t=0 gives

$$S_\infty(1)=\sum_{n=-\infty}^{\infty}\frac{\sin(n+\alpha)}{n+\alpha}=\pi \tag{A21}$$

which implies that

$$S_\infty(x)=\pi \tag{A22}$$

Similarly, when x=1 and K=∞,

$$P_\infty(1)=\sum_{n=-\infty}^{\infty}\frac{\cos(n+\alpha)}{n+\alpha} \tag{A23}$$

Define a function $\chi_2(t)\in L^1_{[-\pi,\pi]}$ with a period of 2π

$$\chi_2(t)=\begin{cases}e^{-j\alpha t}, 0<t<1\\ -e^{-j\alpha t}, -1<t<0\\ 0, otherwise\end{cases} \tag{A24}$$

The Fourier coefficients of $\chi_2(t)$ are calculated as

$$\hat{\chi}_2(n)=\frac{1}{2\pi}\int_{-\pi}^{\pi}\chi_2(t)e^{-jnt}dt=\frac{j}{\pi}\frac{\cos(n+\alpha)}{n+\alpha}-\frac{j}{\pi}\frac{1}{\alpha+n} \tag{A25}$$

Then, $\chi_2(t)$ is represented by the Fourier series as

$$\chi_2(t)=\frac{j}{\pi}\sum_{n=-\infty}^{\infty}\left[\frac{\cos(n+\alpha)}{n+\alpha}-\frac{1}{\alpha+n}\right]e^{jnt} \tag{A26}$$

Based on $\chi_2(0)=0$ and (A6), it is derived that

$$P_\infty(1)=\sum_{n=-\infty}^{\infty}\frac{\cos(n+\alpha)}{n+\alpha}=\pi\cot(\alpha\pi) \tag{A27}$$

Therefore,

$$P_\infty(x)=\pi\cot(\alpha\pi) \tag{A28}$$

Considering the following series

$$B(x)=\sum_{n=-\infty}^{\infty}\frac{e^{j(\alpha+n)x}}{\alpha+n} \tag{A29}$$

it can be rewritten by Euler formula,

$$B(x)=\sum_{n=-\infty}^{\infty}\frac{\cos[(\alpha+n)x]}{\alpha+n}+j\sum_{n=-\infty}^{\infty}\frac{\sin[(\alpha+n)x]}{\alpha+n} \tag{A30}$$

According to (A22) and (A28), (A30) can be rewritten as

$$B(x)=\pi\cot(\alpha\pi)+j\pi=j2\pi\frac{e^{j\alpha\pi}}{e^{j\alpha\pi}-e^{-j\alpha\pi}} \tag{A31}$$

Then, the following equation is established

$$\sum_{n=-\infty}^{\infty}\frac{e^{jnx}}{\alpha+n}=j2\pi\frac{e^{-j\alpha x}e^{j\alpha\pi}}{e^{j\alpha\pi}-e^{-j\alpha\pi}} \tag{A32}$$

The infinite series can be represented as

$$\sum_{n=-\infty}^{\infty}\frac{e^{jn2\pi D}}{s+jn\omega_x}=\frac{1}{j\omega_x}\sum_{n=-\infty}^{\infty}\frac{e^{jn(2\pi D)}}{\frac{\omega}{\omega_x}+n} \tag{A33}$$

According to (A32), (A33) can be deduced as

$$\sum_{n=-\infty}^{\infty}\frac{e^{jn2\pi D}}{s+jn\omega_x}=\frac{2\pi}{\omega_x}\frac{e^{-2D\pi s/\omega_x}e^{\pi s/\omega_x}}{e^{\pi s/\omega_x}-e^{-\pi s/\omega_x}} \tag{A34}$$

Proof is completed.

PROOF OF LEMMA 2

Choose $\Re\{y\}>0$ and define

$$f(t)=\begin{cases}e^{-yt}, t>0\\ 0, t<0\end{cases} \tag{B1}$$

with $f(0)=1/2$. $\Re\{y\}$ denotes the real-part of the complex number y. The n_{th} Fourier coefficient is obtained as

$$\hat{f}(n)=\int_{-\infty}^{\infty}f(t)e^{-jnt}dt=\frac{1}{y+jn} \tag{B2}$$

According to Poisson Summation Formula [36], the following equation is established

$$\sum_{n=-\infty}^{\infty}f(t+2\pi n)=\frac{1}{2\pi}\sum_{n=-\infty}^{\infty}\frac{1}{y+jn}e^{jnt} \tag{B3}$$

Substituting (B1) into (B3) yields

$$\frac{1}{2\pi}\sum_{n=-\infty}^{\infty}\frac{1}{y+jn}e^{jnt}=\sum_{n\geq-\frac{t}{2\pi}}^{\infty}e^{-y(t+2\pi n)}+\begin{cases}\frac{1}{2}, t\in 2\pi\mathbb{Z}\\ 0, otherwise\end{cases} \tag{B4}$$

The infinite series can be expressed as

$$\sum_{n=-\infty}^{\infty}\frac{e^{-jn2\pi D}}{s+\gamma+jn\omega_x}=\frac{2\pi}{\omega_x}\frac{1}{2\pi}\sum_{n=-\infty}^{\infty}\frac{1}{\frac{s+\gamma}{\omega_x}+jn}e^{jn(-2\pi D)} \tag{B5}$$

Based on (B4), (B5) can be rewritten as

$$\sum_{n=-\infty}^{\infty}\frac{e^{-jn2\pi D}}{s+\gamma+jn\omega_x}=\frac{2\pi}{\omega_x}\sum_{n=1}^{\infty}e^{-\frac{s+\gamma}{\omega_x}(-2\pi D+2\pi n)} \tag{B6}$$

The sum of an infinite series of exponential functions is easily derived as

$$\sum_{n=1}^{\infty}e^{-2\pi yn}=\frac{e^{-\pi y}}{e^{\pi y}-e^{-\pi y}} \tag{B7}$$

Therefore, (B6) can be further simplified as

$$\sum_{n=-\infty}^{\infty}\frac{e^{-jn2\pi D}}{s+\gamma+jn\omega_x}=\frac{2\pi}{\omega_s}\frac{e^{2D\pi(s+\gamma)/\omega_x}e^{-\pi(s+\gamma)/\omega_x}}{e^{\pi(s+\gamma)/\omega_x}-e^{-\pi(s+\gamma)/\omega_x}} \tag{B8}$$

Proof is completed.

REFERENCES

[1] D. M. Van de Sype, K. De Gusseme, F. M. L. L. De Belie, A. P. Van den Bossche, and J. A. Melkebeek, "Small-signal z-domain analysis of digitally controlled converters," *IEEE Trans. Power Electron.*, vol. 21, no. 2, pp. 470–478, Mar. 2006.

[2] A. V. Peterchev, J. Xiao, and S. R. Sanders, "Architecture and IC implementation of a digital VRM controller," *IEEE Trans. Power Electron.*, vol. 18, no. 1, pp. 356–364, Jan. 2003.

[3] X. Wang and F. Blaabjerg, "Harmonic stability in power electronic-based power systems: concept, modeling, and analysis," *IEEE Trans. Smart Grid*, vol. 10, no. 3, pp. 2858–2870, May 2019.

[4] D. J. Packard, "Discrete modeling and analysis of switching regulators," Ph. D. dissertation, California Inst. Technol., Pasadena, May 1976.

[5] S. K. Mazumder, A. H. Nayfeh, and D. Boroyevich, "Theoretical and experimental investigation of the fast- and slow-scale instabilities of a DC-DC converter," *IEEE Trans. Power Electron.*, vol. 16, no. 2, pp. 201–216, Mar. 2001.

[6] R. Tymerski, "Frequency analysis of time-interval-modulated switched networks," *IEEE Trans. Power Electron.*, vol. 6, no. 2, pp. 287–295, Apr. 1991.

[7] R. D. Middlebrook, "Input filter considerations in design and application of switching regulators," in *Proc. IEEE Ind. Appl. Soc. Annu. Meeting*, 1976.

[8] R. D. Middlebrook and S. Cuk, "A general unified approach to modeling switching-converter power stages," in *Proc. IEEE Power Electron. Spec. Conf.*, pp. 18–34, Jun. 1976.

[9] V. Vorperian, "Simplified analysis of PWM converter using model of PWM switch, Part I: Continuous conduction mode," *IEEE Trans. Aerosp. Electron. Syst.*, vol. 26, no. 3, pp. 490–496, May 1990.

[10] Y. Yan, F. C. Lee, and P. Mattavelli, "Comparison of small signal characteristics in current mode control schemes for point-of-load Buck converter applications," *IEEE Trans. Power Electron.*, vol. 28, no. 7, pp. 3405–3414, Jul. 2013.

[11] S. R. Sanders, J. M. Noworolski, X. Z. Liu, and G. C. Verghese, "Generalized averaging method for power conversion circuits," *IEEE Trans. Power Electron.*, vol. 6, no. 2, pp. 251–259, Apr. 1991.

[12] J. Groves, "Small-signal analysis using harmonic balance methods," in *Proc. IEEE Power Electronic. Spec. Conf.*, pp. 74–79, 1991.

[13] Y. Wang, D. Gao, D. Tannir, N. Dong, G. P. Fang, W. Dong, and P. Li, "Multiharmonic small-signal modeling of low-power PWM DC-DC converters," *ACM Trans. Des. Autom. Electron. Syst.*, vol. 22, no. 4, pp. 68–83, Jun. 2017.

[14] R. Tymerski, V. Vorperian, F. C. Lee, and W. Baumann, "Nonlinear modeling of the PWM switch," *IEEE Trans. Power Electron.*, vol. 4, no. 2, pp. 225–233, Apr. 1989.

[15] Y. Qiu, M. Xu, K. Yao, J. Sun, and F. C. Lee, "Multifrequency small-signal model for Buck and multiphase interleaving Buck converters," *IEEE Trans. Power Electron.*, vol. 21, no. 5, pp. 1185–1192, Sep. 2006.

This article has been accepted for publication in a future issue of this journal, but has not been fully edited. Content may change prior to final publication. Citation information: DOI 10.1109/TIE.2021.3050389, IEEE Transactions on Industrial Electronics

[16] Y. Qiu, M. Xu, K. Yao, J. Sun, and F. C. Lee, "A generic high-frequency model for the nonlinearities in Buck converters," *IEEE Trans. Power Electron.*, vol. 22, no. 5, pp. 1970–1977, Sep. 2007.

[17] S.-F. Hsiao, D. Chen, C.-J. Chen, and H.-S. Nien, "A new multiple-frequency small-signal model for high-bandwidth computer V-core regulator applications," *IEEE Trans. Power Electron.*, vol. 31, no. 1, pp. 733–742, Jan. 2016.

[18] X. Yue, F. Zhuo, S. Yang, Y. Pei, and H. Yi, "A matrix-based multifrequency output impedance model for beat frequency oscillation analysis in distributed power systems," *IEEE J. Emerg. Sel. Power Electron.*, vol. 4, no. 1, pp. 80-92, Mar. 2016.

[19] X. Li, X. Ruan, Q. Jin, M. Sha, and C. K Tse, "Small-signal models with extended frequency range for DC-DC converters with large modulation ripple amplitude," *IEEE Trans. Power Electron.*, vol. 33, no. 9, pp. 8151–8163, Sep. 2018.

[20] X. Cheng, J. Liu, and Z. Liu, "A generalized multi-frequency small-signal model for high-bandwidth Buck converters under constant-frequency voltage-mode control," *IEEE Trans. Power Electron.*, vol. 35, no. 8, pp. 8186-8199, Aug. 2020.

[21] F. Gonzalez-Espin, E. Figueres, G. Garcera, R. Gonzalez-Medina, and M. Pascual, "Measurement of the loop gain frequency response of digitally controlled power converters," *IEEE Trans. Ind. Electron.*, vol. 57, no. 8, pp. 2785-2796, Aug. 2010.

[22] J. Castello and J. M. Espi, "DSP implementation for measuring the loop gain frequency response of digitally controlled power converters," *IEEE Trans. Power Electron.*, vol. 27, no. 9, pp. 4113-4121, Sep. 2012.

[23] X. Ruan, C. Xiong, X. Li, X. Xiong, Q. Jin, M. Sha, and C. K Tse, "Reconsideration of loop gain and its measurement in DC-DC converters," *IEEE Trans. Power Electron.*, vol. 34, no. 7, pp. 6906-6921, Jul. 2019.

[24] N. M. Wereley, "Analysis and control of linear periodically time varying systems," Ph.D. dissertation, Dept. of Aeronautics and Astronautics, MIT Inst. Technol., Massachusetts, 1991.

[25] E. Mollerstedt, "Dynamic analysis of harmonics in electrical systems," Ph.D. dissertation, Dept. Automatic Control, Lund Inst. Technol., Lund, Sweden, 2000.

[26] G. N. Love and A. R. Wood, "Harmonic state space model of power electronics," in *Proc. Int. Conf. Harmonics Quality Power*, pp. 1–6, 2008.

[27] J. Kwon, X. Wang, F. Blaabjerg, C. L. Bak, V. S. Sularea, and C. Busca, "Harmonic interaction analysis in a grid-connected converter using harmonic state-space (HSS) modeling," *IEEE Trans. Power Electron.*, vol. 32, no. 9, pp. 6823–6835, Sep. 2017.

[28] C. Zhang, M. Molinas, A. Rygg, J. Lyu, and X. Cai, "Harmonic transfer-function-based impedance modeling of a three-phase VSC for asymmetric AC grids stability analysis," *IEEE Trans. Power Electron.*, vol. 34, no.12, pp. 12552–12566, Dec. 2019.

[29] E. Mollerstedt and B. Bernhardsson, "Out of control because of harmonics-An analysis of the harmonic response of an inverter locomotive," *IEEE Control Syst. Mag.*, vol. 20, no. 4, pp. 70–81, Aug. 2000.

[30] X. Yue, X. Wang, and F. Blaabjerg, "Review of small-signal modeling methods including frequency-coupling dynamics of power converters," *IEEE Trans. Power Electron.*, vol. 34, no. 4, pp. 3313–3328, Apr. 2019.

[31] A. V. Oppenheim and R. W. Schafer, *Discrete-Time Signal Processing*, 3rd ed. London, U.K., Pearson Education, 2009.

[32] R. Erickson and D. Maksimovic, *Fundamentals of Power Electronics*, 2nd ed. Norwell, M.A., Kluwer, 2004.

[33] R. Middlebrook, "Measurement of loop gain in feedback systems," *Int. J. Electron.*, vol. 38, no. 4, pp. 485-512, Apr. 1975.

[34] B. H. Cho and F. C. Lee, "Measurement of loop gain with the digital modulator," *IEEE Trans. Power Electron.*, vol. 1, no. 1, pp. 55-62, Jan. 1986.

[35] T. M. Apostol, *Mathematical Analysis*, 2nd ed. London, U.K., Pearson Education, 2009.

[36] J. Borwein, D. Bailey and R. Girgensohn, *Experimentation in Mathematics: Computational Paths to Discovery*. Massachusetts, A K Peters. 2004.

Jianheng Lin was born in Fujian, China, in 1994. He received the B.S. degree in electronic engineering from Jimei University, Xiamen, China, in 2016. He is currently working toward the Ph.D. degree in control science and engineering at the Central South University, Changsha.

His research interests include modeling and control of time periodic system.

Mei Su was born in Hunan, China, in 1967. She received the B.S., M.S. and Ph.D. degrees from the School of Information Science and Engineering, Central South University, Changsha, China, in 1989, 1992 and 2005, respectively. She has been a Full Professor with the School of Automation, Central South University. She is currently an Associate Editor of the IEEE Transactions on Power Electronics.

Her research interests include matrix converter, adjustable speed drives, and wind energy conversion system.

Yao Sun (M'13) was born in Hunan, China, in 1981. He received the B.S., M.S. and Ph.D. degrees from Central South University, Changsha, China, in 2004, 2007 and 2010, respectively. He has been a Professor with the School of Automation, Central South University, China.

His research interests include matrix converter, micro-grid and wind energy conversion system.

Xing Li was born in Hunan, China, in 1988. She received the B.S. and Ph.D. degrees from Central South University, Changsha, China, in 2009 and 2014, respectively. She is currently an Associate Professor with the College of Electrical and Information Engineering, Hunan University, Changsha, China.

Her research interests include power electronic converter and wind energy conversion system.

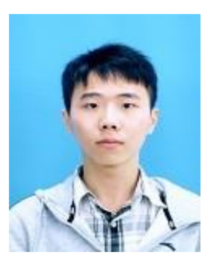

Shiming Xie was born in Fujian, China, in 1995. He received the B.S. degree in electronic engineering from Central South University, Changsha, China, in 2017. He is currently working toward the Ph.D. degree in control science and engineering.

His research interests include matrix converter and modeling and control of power electronics converters.

Guanguan Zhang received the B.Sc. and Ph.D. degrees from Central South University, Changsha, China, in 2012 and 2018, respectively. From 2016 to 2017, she was a joint Ph.D. student with the Department of Energy Technology, Aalborg University, Aalborg, Denmark, where she focused on the reliability analysis of wind power systems. Since 2018, she is a Postdoctoral Research Fellow with the School of Control Science and Engineering, Shandong University, Jinan, China.

Her research interests include control, applications, and reliability of power converters and wind energy generation.

Frede Blaabjerg (Fellow, IEEE) received the Ph.D. degree in electrical engineering from Aalborg University, Aalborg, Denmark, in 1995.

From 1987 to 1988, he was with ABB-Scandia, Randers, Denmark, He became an Assistant Professor in 1992, an Associate Professor in 1996, and a Full Professor of power electronics and drives in 1998. In 2017, he became a Villum Investigator. He is honoris causa at the University Politehnica Timisoara, Romania, and Tallinn Technical University, Tallinn, Estonia. He has authored or coauthored more than 600 journal papers in the fields of power electronics and its applications. He is the co-author of four monographs and an editor of ten books in power electronics and its applications. His current research interests include power electronics and its applications, such as in wind turbines, PV systems, reliability, harmonics, and adjustable speed drives.

Prof. Blaabjerg was the recipient of 32 IEEE Prize Paper Awards, the IEEE PELS Distinguished Service Award in 2009, the EPE-PEMC Council Award in 2010, the IEEE William E. Newell Power Electronics Award 2014, the Villum Kann Rasmussen Research Award 2014, the Global Energy Prize in 2019, and the 2020 IEEE Edison Medal. He was the Editor-in-Chief for the IEEE TRANSACTIONS ON POWER ELECTRONICS from 2006 to 2012. He was a Distinguished Lecturer for the IEEE Power Electronics Society from 2005 to 2007 and for the IEEE Industry Applications Society from 2010 to 2011 as well as from 2017 to 2018. From 2019 to 2020, he serves as a President of IEEE Power Electronics Society. He is Vice-President of the Danish Academy of Technical Sciences. He is nominated in 2014-2019 by Thomson Reuters to be between the 250 most-cited researchers in Engineering in the world.

Jianghua Feng was born in Hengyang, China, on November, 19, 1964. He received the B.S. degree and the M.S. degree in Electric Machine and Control from Zhejiang University, Hangzhou, China respectively in 1986 and 1989 and his Ph.D. degree in Control Theory and Control Engineering from Central South University, Changsha, China in 2008. In 1989, he joined the staff of CSR Zhuzhou Institute Co. Ltd., Zhuzhou, China, where he is CTO since 2010.

His research interest is electrical system and its control in rail transportation field, and now is a professorate senior engineer and has several journal papers published in Proceedings of China Internat, IEEE International Symposium on Industrial Electronics, International Power Electronics and Motion Control Conference, IEEE Conference on Industrial Electronics and Applications, IPEC, IECON, ICEMS.